

A Collaborative Model-driven Network for MRI Reconstruction

Xiaoyu Qiao, Weisheng Li, Guofen Wang, and Yuping Huang

arXiv:2402.03383v1 [eess.IV] 4 Feb 2024

Abstract—Magnetic resonance imaging (MRI) is a vital medical imaging modality, but its development has been limited by prolonged scanning time. Deep learning (DL)-based methods, which build neural networks to reconstruct MR images from undersampled raw data, can reliably address this problem. Among these methods, model-driven DL methods incorporate different prior knowledge into deep networks, thereby narrowing the solution space and achieving better results. However, the complementarity among different prior knowledge has not been thoroughly explored. Most of the existing model-driven networks simply stack unrolled cascades to mimic iterative solution steps, which are inefficient and their performances are suboptimal. To optimize the conventional network structure, we propose a collaborative model-driven network. In the network, each unrolled cascade comprised three parts: model-driven subnetworks, attention modules, and correction modules. The attention modules can learn to enhance the areas of expertise for each subnetwork, and the correction modules can compensate for new errors caused by the attention modules. The optimized intermediate results are fed into the next cascade for better convergence. Experimental results on multiple sequences showed significant improvements in the final results without additional computational complexity. Moreover, the proposed model-driven network design strategy can be easily applied to other model-driven methods to improve their performances.

Index Terms—attention mechanism, low-rankness, MRI reconstruction, model-driven, sparsity.

I. INTRODUCTION

Magnetic resonance imaging (MRI) is an irreplaceable imaging modality [1], which has been widely used in clinical scenarios. However, the acquisition of full-sampled raw k-space data is inherently time-consuming. This aggravates patient discomfort and produces artifacts on MR images, limiting the development and application of MR imaging.

To address this problem, parallel imaging (PI) [2], which uses multiple receiving coils to acquire MR signals, has been widely employed in clinical scenarios. PI methods are classified into two main categories: elimination of aliasing

This work was supported by the National Natural Science Foundation of China [Nos. 62331008, 61972060, 62027827 and 62221005], National Key Research and Development Program of China (Nos. 2019YFE0110800), Chongqing University of Posts and Telecommunications ph.D. Innovative Talents Project [BYJS202211]. (Corresponding author: Weisheng Li)

X. Qiao, W. Li and Y. Huang are with Chongqing Key Laboratory of Image Cognition, Chongqing University of Posts and Telecommunications, Chongqing, 400065, China. (email: liws@cqupt.edu.cn)

G. Wang is with College of Computer and Information Science, Chongqing Normal University, Chongqing, 401331, China.

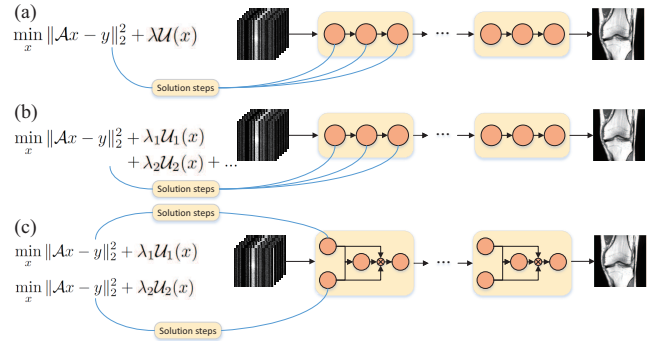


Fig. 1. (a) conventional model-driven network structure. (b) common modification in model-driven networks. (c) our proposed network structure.

artifacts in the image domain, which is represented by the SENSE [3] algorithm; and interpolation in the k-space domain, which is represented by the GRAPPA [4] algorithm. In addition to PI, compressed sensing (CS) theory [5], [6], which is highly compatible with the MR imaging background, has also been applied to MR image reconstruction [7], [8]. The CS theory enables the reconstruction of MR images from highly undersampled k-space data, which violates the Nyquist-Shannon sampling theorem. The sparsity of the k-space data in the transform domains is typically exploited to narrow the solution space. Iterative optimization algorithms are then leveraged to approach the target MR images.

Conventional approaches are limited by issues such as long computation times, low acceleration rates, and suboptimal performance [9], [10]. Considering the significant progress made by deep learning (DL) methods in computer vision tasks, DL-based methods have been successfully introduced into the MRI reconstruction field, which can be broadly categorized into data-driven and model-driven methods [11]. Data-driven methods [12]–[17] use deep networks to build a pipeline between the inputs (undersampled k-space data or aliased images) and outputs (fully sampled data or artifact free images). In comparison, model-driven methods [18]–[29] can be viewed as combinations of conventional and data-driven methods. Prior knowledge is integrated into model-driven networks, whereas deep-learning methods can learn more complex feature representations through learning processes. More specifically, the solution steps of conventional algorithms are unrolled into deep networks, as shown in Fig. 1 (a). For example, Zhang [19] *et al.* proposed ISTA-Net that unfolds the update steps of ISTA [30] into a deep network.

The sparsity transform and its inverse version in ISTA were learned in the network, and a loss function was designed to fulfil the symmetry constraint. In contrast, Duan [20] *et al.* developed a variable-splitting method to solve the objective function and incorporated the corresponding three-step update process into the network. Sriram [21] *et al.* extended the Variational Network [22] and fulfilled the update steps in k -space by learning end-to-end. Yiasemis [23] *et al.* explored the applied Convolutional Recurrent Neural Networks (CRNNs) to an unrolled network to solve the inverse problem.

In addition to sparsity [31], low rankness is being increasingly applied in inverse problems [32]–[41]. For example, Ke [35] *et al.* leveraged low-rank priors to improve sparsity-driven DL-based reconstruction methods. By considering the temporal frames in dynamic MRI as columns of a spatiotemporal matrix, low-rank properties can be utilized. For static MRI reconstruction, low-rank Hankel matrix (LRHM) [42] and LRHM factorization (LRHMF) methods were routinely used [43]. For example, Zhang [36] *et al.* proposed the exploration of simultaneous two-directional low-rankness (STDLR) in k -space data and used an SVD-free algorithm [44] to reduce computation time. Then, alternating direction method of multipliers (ADMM)-based [45] methods were used to minimize the objective function. Some methods use structured low-rank (SLR) [37], [38] algorithms to reduce the computational complexity in completing the Hankel matrix. For example, Pramanik [39] *et al.* proposed a general SLR-based network that significantly reduced the computational complexity. Zhang [40] *et al.* constrained the low rankness of rows and columns of k -space data to reduce computational complexity, and they alleviated the reconstruction errors by introducing prior information. Wang [41] *et al.* split a 2D reconstruction problem into several 1D reconstructions and constructed cascaded Hankel matrices on 1D hybrid data.

A common way to optimize model-driven methods is to incorporate different regularizers into the objective functions to narrow the solution space more precisely (Fig. 1 (b)). Some methods [46]–[49] simultaneously incorporated prior knowledge, such as sparsity and low rankness, in dynamic MRI considering the image characteristics. In DL-based reconstruction methods [35], [41], objective functions designed with sparsity- and low-rankness-based regularizers were used to build a network based on a corresponding iterative algorithm. In addition to explicit prior knowledge, some methods also proposed to impose constraints from learned sensitivity maps for accurate reconstructions [27], [50]. However, the existing methods have not explored the way of fully exploiting the complementarity of different types of priors. Most model-driven methods are designed to stack unrolled cascades, and different priors can then aid in network training in an alternative form. We believe the network design is inefficient, and their reconstruction performance is suboptimal. Instead, we aim to propose a parallel network structure that different branches in the network can simultaneously contribute to the training process to achieve better results. Therefore, we designed a new strategy for designing model-driven networks (Fig. 1 (c)). Our objective is to find the areas of expertise of the subnetworks based on different priors to further optimize

intermediate results and seek better convergence. Alternatively, from a macro-perspective, we can easily determine the global optimum by appropriately integrating different priors into the network.

The proposed network is called a collaborative model-driven network (CMD-Net). In the proposed network, subnetworks based on sparsity and low rankness are effectively integrated using an attention module to achieve better performances. Correction modules are connected to the optimized weighted images, providing considerable flexibility to compensate for newly introduced errors. Data consistency modules were used to maintain consistency with the known sampling information. Although the subnetworks are established by stacking the unrolled cascades of iterative algorithms, the optimized intermediate results from the last cascade are used to replace the inputs of the next cascade to facilitate network convergence. Moreover, the intermediate results from different modules are directly input into the loss function to constrain their functions. The experimental results show that the proposed method outperforms one-prior and traditional multiprior-based networks. Compared with the state-of-the-art methods, our method also yields better results. Furthermore, the proposed method is compatible with other model-driven networks having different priors or objective functions. The experimental results show that using the proposed strategy, the performance of different model-driven networks can be improved without increasing computational complexity.

The contributions of this study are summarized as follows:

- 1) We propose a collaborative model-driven MRI reconstruction network design strategy, which effectively integrate sub-networks based on different priors.
- 2) Experimental results on multiple sequences show that the proposed method can achieve better performance without extra computational complexity.
- 3) The proposed network design strategy can be easily applied to other model-driven network and significantly improve their performance.

II. PROBLEM FORMULATION

In this study, we focused on reconstruction under the PI scenario. The undersampled k -space measurement $y \in \mathbb{C}^{NC}$ is represented by

$$y = Ax + b \quad (1)$$

where $x \in \mathbb{C}^N$ is the unknown MR image to be reconstructed and b is the measurement noise. Here, $N = H \times W$, where H and W are the length and width of y , respectively, and C is the coil number. $\mathcal{A}(\cdot)$ denotes the sampling matrix that is

$$\mathcal{A}(\cdot) = \mathcal{P} \circ \mathcal{F} \circ \mathcal{E}(\cdot) \quad (2)$$

for PI. Here, $\mathcal{P}(\cdot)$ denotes the undersampling matrix, $\mathcal{F}(\cdot)$ denotes the Fourier transform, $\mathcal{E}(\cdot)$ is the expanding operator [21], [23] given as

$$\mathcal{E}(x) = \{\mathcal{S}_1 x, \mathcal{S}_2 x, \dots, \mathcal{S}_i x\}, i = 1, 2, \dots, C \quad (3)$$

that applies sensitivity maps to x to generate coil-specific images. \mathcal{S}_i denotes the sensitivity matrix of the i th coil. In

contrast, the reduced operator is given by

$$\mathcal{R}\{x_1, x_2, \dots, x_L\} = \sum_{i=1}^C \mathcal{S}_i \otimes x_i, i = 1, 2, \dots, C \quad (4)$$

that integrates the coil images into one image. Hence, the Hermitian transposition of $\mathcal{A}(\cdot)$ is given by:

$$\mathcal{A}^*(\cdot) = \mathcal{R} \circ \mathcal{F}^{-1} \circ \mathcal{P}(\cdot) \quad (5)$$

To reconstruct the MR images from measurement y , the objective function is given as

$$\hat{x} = \arg \min_x \sum_{i=1}^C \|\mathcal{P}\mathcal{F}\mathcal{S}_i x - y\|_2^2 + \lambda \mathcal{U}(x) \quad (6)$$

where the first polynomial is a data fidelity term and the second term denotes different regularizers that incorporate prior information to narrow the solution space. λ was used as a regularization parameter to determine the balance. For example, we express (6) as follows:

$$\hat{x} = \arg \min_x \sum_{i=1}^C \|\mathcal{P}\mathcal{F}\mathcal{S}_i x - y\|_2^2 + \lambda_1 \|\Phi(x)\|_1 \quad (7)$$

in sparsity-based algorithms. Φ is an appropriate transformation field for ensuring the sparsity of the raw data. In this study, we aimed to demonstrate the generality and efficiency of the proposed network design strategy. Therefore, we adopted an ISTA-based backbone to solve (7), which iterates between the following two steps:

$$r_s^k = x^{k-1} - \alpha^k \mathcal{A}^*(\mathcal{A}(x^{k-1}) - y) \quad (8)$$

$$x_s^k = \tilde{\mathcal{F}}(\text{soft}(\mathcal{F}(r_s^k), \lambda_1)) \quad (9)$$

where k denotes the k th iteration, α^k is the step size, $\mathcal{F}(\cdot)$ is a learned transformation field to ensure improved sparsity, $\tilde{\mathcal{F}}(\cdot)$ is its inverse operator constrained by a customized loss function, and λ_1 is the shrinkage threshold.

For a low-rankness-based method, (6) can be expressed as

$$\hat{x} = \arg \min_x \sum_{i=1}^L \|\mathcal{P}\mathcal{F}\mathcal{S}_i x - y\|_2^2 + \lambda_2 \|\tau(x)\|_* \quad (10)$$

where $\tau(\cdot)$ is the lifting operator used to construct hankel matrices. $\tau(x)$ is a block hankel matrix with dimensions $Cp_1p_2 \times ((H-p_1+1)(W-p_2+1))$, where p_1 and p_2 are pencil parameters. Singular value decomposition is routinely used to solve nuclear norms; however, it is computationally intensive and time-consuming. As an alternative, some studies leveraged the matrix factorization technique [40]. Some researchers have adopted the iterative reweighted least-squares scheme [39], [41], [51] to majorize the nuclear norm, which can be expressed as

$$\|\tau(x)\|_* \leq \|\tau(x)Q\|_F^2 \quad (11)$$

where Q is the null space of $\tau(x)$ given by

$$Q = [(\tau(x))^H (\tau(x)) + \epsilon I]^{-\frac{1}{4}} \quad (12)$$

$\|\cdot\|_F^2$ denotes the Frobenius norm. We can then solve (10) by alternating between the following two steps.

$$\hat{x}^k = \arg \min_x \sum_{i=1}^C \|\mathcal{P}\mathcal{F}\mathcal{S}_i x^{k-1} - y\|_2^2 + \lambda_2 \|\tau(x^{k-1})Q^{k-1}\|_F^2, \quad (13)$$

$$Q^k = [(\tau(x^{k-1}))^H (\tau(x^{k-1})) + \epsilon I]^{-\frac{1}{4}} \quad (14)$$

we extracted x^k from the lifting operator by leveraging the commutativity of the convolutions [39] as

$$\|\tau(x)Q\|_F^2 = \|\mathcal{D}(Q)x\|_F^2 \quad (15)$$

where $\mathcal{D}(Q)$ is constructed by vertically cascading $\mathcal{D}(q_j)$. q_j is the j -th column of matrix Q and $\mathcal{D}(q_j)$ is a block Hankel matrix constructed from the elements of q_j . Thus, we can rewrite (13) as follows:

$$\hat{x}^k = \arg \min_x \sum_{i=1}^C \|\mathcal{P}\mathcal{F}\mathcal{S}_i x^{k-1} - y\|_2^2 + \lambda_2 \|\mathcal{D}(Q^{k-1})x^{k-1}\|_F^2, \quad (16)$$

and inspired by previous studies [41], [52], [53], we solve (16) by iterating the following two steps:

$$r_l^k = \lambda_2 (\mathcal{D}(Q^{k-1}))^H \mathcal{D}(Q^{k-1}) x^{k-1} \quad (17)$$

$$x_l^k = x^{k-1} - \beta^k (\mathcal{A}^*(\mathcal{A}(x^{k-1}) - y) + 2r_l^k) \quad (18)$$

III. METHOD

A. Network Structure

The proposed network structure and its components are illustrated in Fig. 2. Fig. 2 (a) shows the overall network structure. In the network training process, the undersampled k-space data $y \in \mathbb{C}^{NC}$ as well as the corresponding sensitivity maps $\mathcal{S} \in \mathbb{C}^{NC}$ and masks $\mathcal{P} \in \mathbb{R}^N$ are fed to the network. MR images are stored using complex values, and some studies have proposed complex convolutions [13] to achieve better results; however, this is not our focus. Therefore, two channels were used to store the real and imaginary parts in this study, and $y \in \mathbb{C}^{NC}$, $\mathcal{S} \in \mathbb{C}^{NC}$ were transferred to $y \in \mathbb{R}^{2NC}$, $\mathcal{S} \in \mathbb{R}^{2NC}$ before they are fed into the network. Besides, the coil-combined image x_0 is obtained from the measurement y and fed to the network. Then, several iteration blocks were cascaded to form the main body, and each block is referred to as a cascade. Through stacked cascades, the network finally outputs the reconstructed MR images. The final and intermediate results were fed into the customized loss function introduced in Section 3.5. Each cascade comprised three parts: model-driven subnetworks (green blocks), attention-based fusion modules (yellow blocks), and correction modules (blue blocks). Fig. 2 (b)–(e) present the detailed structures of the modules, which are introduced in the following subsections.

B. Model-driven Sub-networks

In this study, we proposed the proper integration of different types of prior knowledge into the network to achieve better performance. We planned to choose prior knowledge commonly used in model-driven networks to ensure the universality and effectiveness of the network. Moreover, we believe

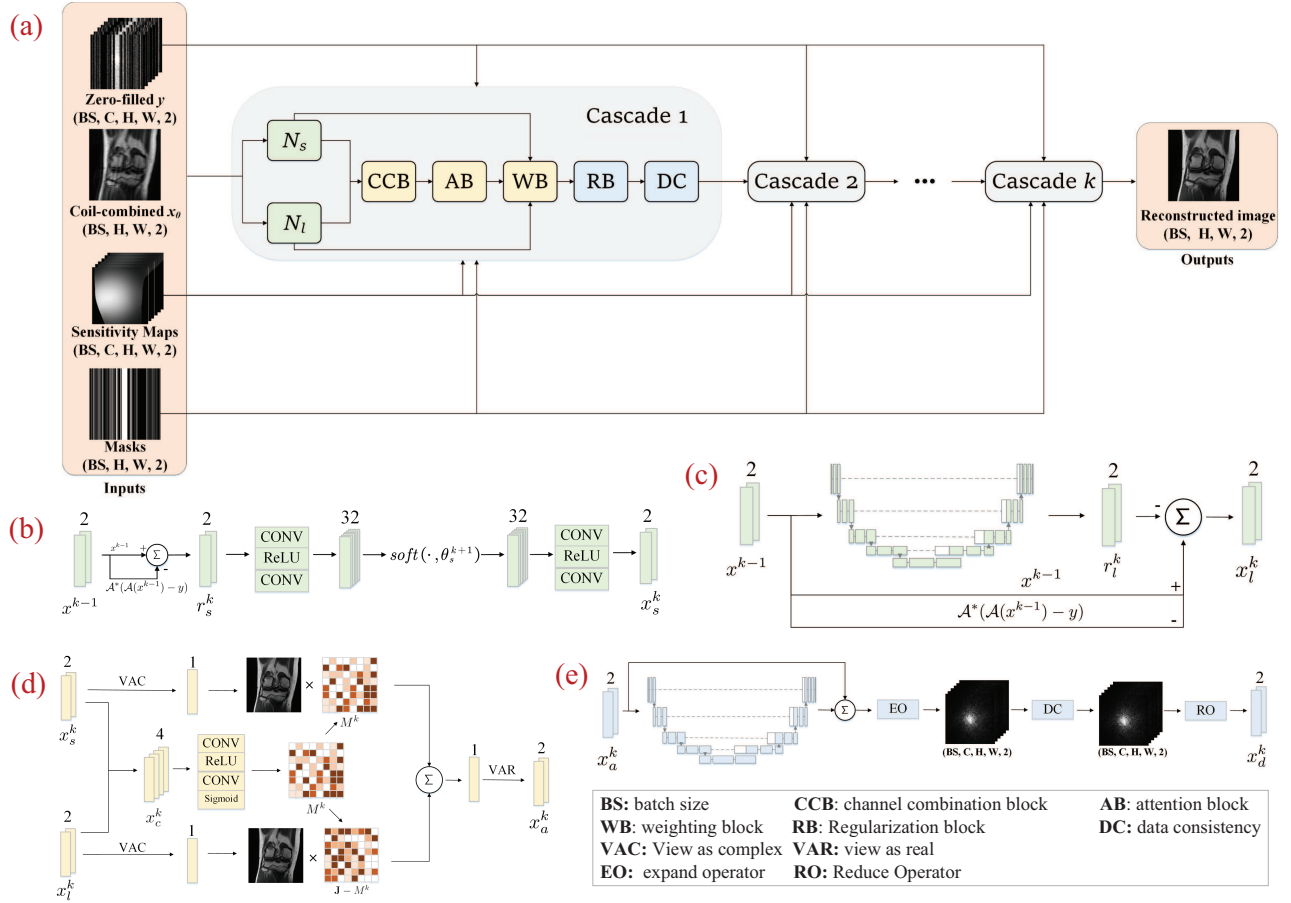


Fig. 2. (a): the structure of the proposed network. (b): the structure of the sparsity based sub-network (N_s in (a)). (c): the structure of the low-rank based sub-network (N_l in (a)). (d): the structure of the attention modules (the yellow blocks in (a)), each of which include a channel combination block (CCB), an attention block (AB), and a weighting block (WB). (e): the structure of the correction modules (the blue blocks in (a)), each of which includes a regularization block (RB) and a data consistency block.

that there is a better complementarity between different types of prior knowledge than the same knowledge, which can be exploited. Therefore, we designed a sparsity-based subnetwork (N_s in Fig. 2) and low-rankness-based subnetwork (N_l in Fig. 2). For N_s , we adopted the sparsity-based ISTA-Net as the backbone network. The learned $\mathcal{F}(\cdot)$ and $\tilde{\mathcal{F}}(\cdot)$ are implemented using cascaded convolutional layers and ReLU activation functions, as shown in Fig. 2 (b). We noted that the output of N_s in the k th iteration is x_s^k , and we have

$$x_s^k = N_s(x^{k-1}), \quad (19)$$

and N_s denotes the iterative processes in (8) and (9).

N_l in each cascade is constructed by unrolling (17) and (18) into the network. For (17), essentially $(\mathcal{D}(Q))^H \mathcal{D}(Q)x$ can be regarded as a projection acting on x , which is determined by Q , and Q at each iteration will also be updated according to the status of x . Therefore, we relaxed the constraint on (17) and used U-Net to learn the mapping directly, as shown in Fig. 2 (c). By doing so, we avoided a complicated calculation process, and more accurate intermediate variables can be learned directly from the data. We used N_{lu} to represent U-Net, and thus, we have

$$r_l^k = \lambda_2 N_{lu}(x^{k-1}) \quad (20)$$

Similar to (19), we obtained

$$x_l^k = N_l(x^{k-1}) \quad (21)$$

where N_l denotes the processes in (20) and (18), respectively.

Notably, the proposed model-driven subnetworks differ from another previously proposed method [41] that also involves sparsity and low-rank priors. First, they proposed decoupling the 2D Fourier transform into two 1D processes, and then obtained much more data to train the network, while greatly reducing the computational complexity. However, our purpose was to design a universal model-driven network that can be easily generalized. Therefore, we still adopted a 2D reconstruction process. More importantly, we do not place both regularizers into a single objective function, which is

$$\hat{x} = \arg \min_x \sum_{i=1}^C \|\mathcal{P}\mathcal{F}\mathcal{S}_i x - y\|_2^2 + \lambda_1 \|\Phi(x)\|_1 + \lambda_2 \|\tau(x)\|_* \quad (22)$$

The corresponding model-driven network was built based on the solution steps. As an alternative, we place different regularizers based on different priors into two objective functions (i.e., (7) and (10)). Hence, two subnetworks are built. In our opinion, the iterative steps for solving (22) essentially incorporate the information learned from regularizers into



coronal PD 4x

Fig. 3. From left to right: a fully sampled MR image, a zero-filled undersampled MR image and the corresponding sampling mask. The first row: 4-fold acceleration. The second row: 6-fold acceleration.

the training step in an alternating form. For comparison, we aimed to effectively integrate the intermediate results from different subnetworks and make different branches simultaneously contribute to the training process. By doing so, different subnetworks can help each other achieve faster convergence. We conducted experiments in Section 4.3 to compare the two aforementioned methods. Then, we propose an attention module to organically integrate the subnetworks, which is introduced in the next subsection.

C. Attention Module

The attention module (ATM) includes all the yellow blocks in Fig. 2; the details are shown in Fig. 2 (d). The two inputs are $x_s^k \in \mathbb{R}^{2N}$ and $x_l^k \in \mathbb{R}^{2N}$, which are the outputs of N_s and N_l in the k th cascade. An ATM aims to find better intermediate results for x_s^k and x_l^k for each data point. To achieve this, we first propose a channel combination block (CCB) to concatenate x_s^k and x_l^k on the channel dimensions, and we denote the combined result as $x_c^k \in \mathbb{R}^{4N}$. Then, x_c^k is fed into an element-wise attention block comprising two convolutional layers, each of which connects to an activation layer. We chose the ReLU and sigmoid functions. After the four-layer attention block, we obtained an attention map $M^k \in \mathbb{R}^N$, where each element in M^k lies between zero and one. We transferred x_s^k and x_l^k back to complex values (i.e., $x_s^k, x_l^k \in \mathbb{R}^{2N} \rightarrow x_s^k, x_l^k \in \mathbb{C}^N$) and then created a Hadamard product between M^k and x_s^k, x_l^k is similarly multiplied by $\mathbf{J} - M^k$. $\mathbf{J} \in \mathbb{R}^N$ is a matrix filled with one. We used N_a to represent the weighting block, and the weighted output is given by

$$x_a^k = N_a(x_s^k, x_l^k) = x_s^k \odot M^k + x_l^k \odot (\mathbf{J} - M^k) \quad (23)$$

Therefore, the closer the number in M^k is to 1, the higher the value in x_s^k at the same place occupied in x_a^k . To directly

supervise the attention module, x_a^k explicitly contributes to the loss function. Therefore, the attention module assigns more weights to the subnetwork on the data points that perform better.

D. Correction Module

Through ATMs, the data points on MR images reconstructed by proper subnetworks can have larger weights, and the gap between intermediate outputs and targets can be narrowed. However, this process may introduce new errors owing to inaccurate weights. Therefore, we propose a correction module to revise the errors caused by ATMs. Each correction module consists of a regularizer block (RB) and a data consistency (DC) block. RBs are designed to correct the intermediate results in the image domain and DC blocks in k-space, so that we can fully exploit the complementarity between cross-domain information.

First, a RB block is designed to enhance the network learning ability and provide more flexibility, which is

$$x_r^k = x_a^k + N_r(x_a^k) \quad (24)$$

where N_r is implemented by a U-Net backbone. We design a residual structure to make N_r directly learn the information to be corrected. Unlike subnetworks, conventional prior knowledge is not explicitly or implicitly involved in narrowing the solution space, where RBs learn directly from data. To eliminate new errors, we placed a data consistency (DC) block after U-Net. The DC block is widely used in MR reconstruction models to maximize the use of sampled data to revise the reconstructed results, which is given as

$$x_d^k = \begin{cases} x_r^k, & \text{for undersampled data} \\ \frac{x_r^k + \mu y}{1 + \mu}, & \text{for sampled data} \end{cases} \quad (25)$$

For the sampled data point, a learned μ is used to adjust its ratio with the measurement y . In this way, the regularizer and DC block find a balance during the training process, while the ATMs and correction module also find a balance, which improves the reconstruction performance. Finally, the optimized x_d^k , instead of x_s^k and x_l^k , is fed into the $(k+1)$ th N_s and N_l blocks, which helps the network achieve faster convergence.

Finally, we use N_c to represent the processes in (24) and (25) and obtain $x_d^k = N_c(x_a^k)$. Here, x_d^k is equal to x^{k+1} , and is fed into the next cascade. Therefore, we have:

$$\begin{aligned} x^k &= N_c(x_a^k) = N_c(N_a(x_s^k, x_l^k)) \\ &= N_c(N_a(N_s(x^{k-1}), N_l(x^{k-1}))) \end{aligned} \quad (26)$$

E. Settings and Loss Function

We set the cascade number to 10 in the network. $\alpha^k, \beta^k, \lambda_1, \lambda_2$ were directly learned in the network. For N_s , the number of channels in the convolutional layers was set to 32, 32 in $\mathcal{F}(\cdot)$, and 32, 2 in $\tilde{\mathcal{F}}(\cdot)$. For U-Net in N_l , the number of pooling layers was set to four and the number of channels was set to 16, 32, 64, and 128. For the convolutional layers in ATMs, the number of channels was set to 32 and 1. For U-Net in the

TABLE I
THE QUANTITATIVE RESULTS ON CORONAL PD AND CORONAL PDFS SEQUENCES COMPARED WITH THE STATE-OF-THE-ART METHODS.

Sequence	Method	PSNR		SSIM	
		4x	6x	4x	6x
Coronal PD	zero-filled	31.3089±3.3939	30.5176±3.3902	0.8778±0.0713	0.8626±0.0799
	TV	33.7498±3.1753	32.3290±3.2159	0.8851±0.0657	0.8658±0.0725
	U-Net	36.8984±2.7072	34.7352±2.7863	0.9361±0.0610	0.9133±0.0682
	D5C5	38.7903±2.8408	35.9697±2.7990	0.9509±0.0587	0.9259±0.0689
	ISTA-Net	39.2910±2.8423	35.5220±3.0915	0.9471±0.0567	0.9138±0.0717
	VS-Net	40.1649±2.8767	37.0604±2.7927	0.9591±0.0569	0.9358±0.0648
	E2E-VarNet	39.3592±2.9368	36.8949±3.3872	0.9542±0.0662	0.9342±0.0775
	ReVarNet	40.2545±2.8766	37.3683±2.7869	0.9590±0.0588	0.9379±0.0677
	CMD-Net (ours)	40.9309±2.9400	38.0438±2.8931	0.9637±0.0558	0.9438±0.0660
Coronal PDFS	zero-filled	32.0299±2.0273	31.2221±2.0575	0.7964±0.0998	0.7587±0.1172
	TV	33.7256±1.9058	32.7328±1.8850	0.8124±0.0752	0.7920±0.0796
	U-Net	34.4367±0.6572	33.2028±2.5662	0.8183±0.0106	0.7758±0.1222
	D5C5	34.9671±2.8261	33.4189±2.4765	0.8250±0.1106	0.7854±0.1223
	ISTA-Net	34.4990±2.6389	33.4569±2.5758	0.8198±0.1066	0.7854±0.1214
	VS-Net	34.6847±2.7134	33.5010±2.6100	0.8259±0.1073	0.7842±0.1229
	E2E-VarNet	34.6274±2.7331	33.1626±2.4742	0.8234±0.1101	0.7804±0.1244
	ReVarNet	34.8522±2.7461	33.3146±2.5604	0.8272±0.1080	0.7832±0.1232
	CMD-Net (ours)	35.6337±2.9886	34.2473±2.8743	0.8423±0.1098	0.8001±0.1264

TABLE II
FLOPS OF DIFFERENT MODEL-DRIVEN NETWORKS.

Networks	FLOPs(G)
D5C5	186.55
ISTA-Net	120.13
VS-Net	265.89
E2E-VarNet	187.39
ReVarNet	204.87
CMD-Net (ours)	204.46

correction modules, the number of pooling layers was set to 4, and the number of channels was set to 4, 8, 16, and 32. We greatly reduced the number of channels to save computational resources while maintaining depth to obtain deep features, which is of great significance for correcting the intermediate results.

The experiments were conducted on an RTX 3090 GPU. During training, the batch size was set to 1, and the learning rate was set to 1e-3.

The mean squared error (MSE) was adopted to train the network, expressed as

$$\mathcal{L}_{MSE}(x_g, \hat{x}) = \sum_{i=1}^T \frac{1}{T} \|x_g - \hat{x}\|_2^2 \quad (27)$$

where x_g is the target image (ground truth), \hat{x} is the predicted image, and T is the total amount of training data. The final output of the network and the intermediate components from each cascade are fed to the loss function to supervise the corresponding modules:

$$\begin{aligned} \mathcal{L} = & \gamma_1 \sum_{i=1}^m (x_g, x_s^k) + \gamma_2 \sum_{i=1}^m (x_g, x_l^k) \\ & + \gamma_3 \sum_{i=1}^m (x_g, x_a^k) + \gamma_4 \sum_{i=1}^m (x_g, x_d^k) \\ & + \gamma_5 \sum_{i=1}^m \|\tilde{\mathcal{F}}(\mathcal{F}(r_s^k)) - r_s^k\|_2^2 \end{aligned} \quad (28)$$

where m is the number of stacked cascades. In this study, γ_1 , γ_2, γ_3 and γ_4 were all set to 1 to obtain a faster convergence, and γ_5 , which was used to fulfil the symmetry constraint, was set to 0.01.

IV. EXPERIMENTAL RESULTS

In this section, we compare the proposed network with the state-of-the-art methods to demonstrate its superiority. Ablation studies were conducted to demonstrate the benefits of the proposed modules.

A. datasets

In this study, we followed previous works [20], [22], [39] and used a knee dataset to conduct our experiments, which consist of five sequences: Coronal proton density (PD), coronal fat-saturated PD (PDFS), axial fat-saturated T2, Sagittal fat-saturated T2, Sagittal PD. Each sequence included magnetic resonance (MR) images from 20 patients, each consisting of approximately 40 slices. In this study, the ratio of the training, validation, and testing data was set to 6:2:2. None of the validation or testing data was used for training, and vice versa.

We also conducted our experiments on the fastMRI dataset [54]. Considering the limitation of our training device, we trained the networks on a subset of the fastMRI knee dataset. More specifically, 1146 slices from 50 volumes were used to train the networks with the image size of 640×368 . Because the fastMRI dataset did not provide the fully sampled test data, we split the validation set into a test set and a new validation set. During training, 117 slices from 5 volumes were used for validation. Finally, 949 slices from another 50 volumes were used to evaluate the network performance. All the data were randomly selected and there was no overlapping among them.

For both dataset, we applied Cartesian undersampling with 4-fold and 6-fold acceleration to the k-space data, sampling 24 lines at the central region. A sample MR image and the corresponding sampling masks are shown in Fig. 3. For the first knee dataset, the coil sensitivity maps were pre-computed

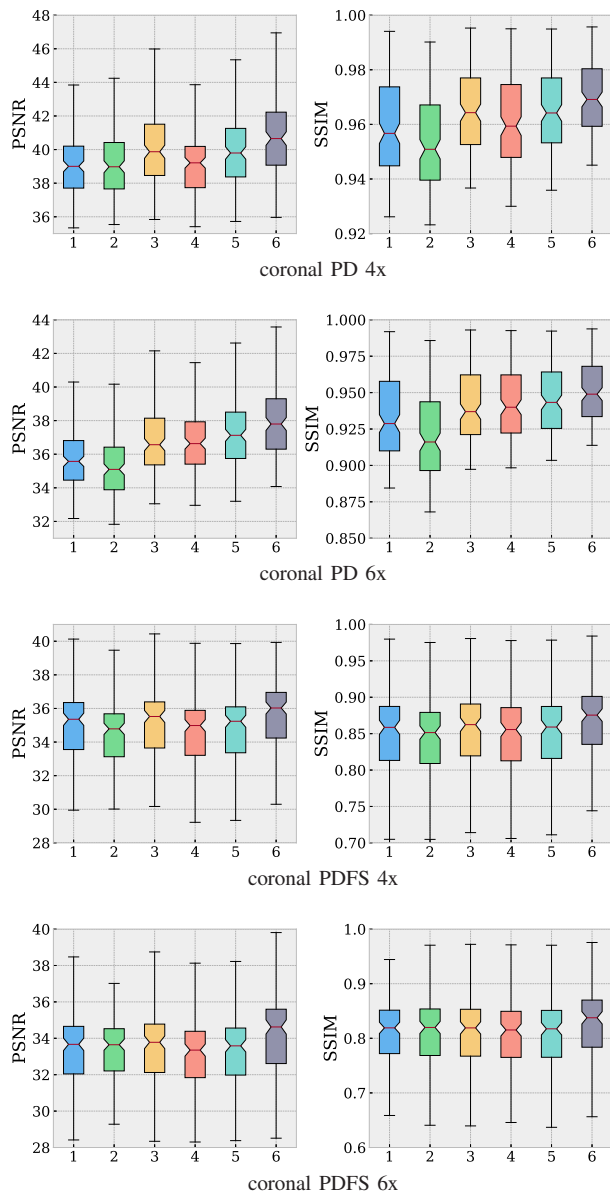


Fig. 4. Box plots of the PSNR and SSIM results on coronal PD and coronal PDFS sequences. Method 1 to 6 are D5C5, ISTA-Net, VS-Net, E2EVarNet, ReVarNet, and CMD-Net(ours).

using ESPIRiT [55], which are provided in the dataset. For fastMRI dataset, we pre-computed the corresponding sensitivity maps using the Sigpy [56] toolbox. More detailed data collection parameters of the aforementioned dataset can be found in the corresponding papers [22], [54].

B. Comparison with related methods

We compared the performance of our network with some representative related methods, and the results are shown in Table I. Experiments were conducted on Coronal PD and PDFS sequences. We tested $4\times$ and $6\times$ accelerations, which means that we sampled a quarter and a sixth of the raw data as the network inputs, respectively. We used the most commonly used PSNR and SSIM metrics to evaluate the performances of the different networks. In the table, the zero-filled method

denotes the baseline results, where the undersampled raw data are filled with zeros. TV denotes the conventional total variation algorithm [57]. U-Net denotes the basic U-Net structure. The number of pooling layers was set to 4, and the number of corresponding channels were set to 32, 64, 128, and 256. D5C5 [58], ISTA-Net [19], VS-Net [20], E2E-VarNet [21], and ReVarNet [23] are recently proposed model-driven networks.

Considering that the computational complexity of different networks varies significantly, which subsequently affects the reconstruction results, we sought to unify the floating-point operations (FLOPs) of different networks for a fair comparison, as shown in Table II. As the cascade number is significant for achieving superior reconstruction performance, we appropriately modified the number of channels to reduce computational complexity. We reduced the number of channels in ReVarNet from 64 to 32 to reduce the number of FLOPs to the same level as in the other models. Considering that D5C5 had lower FLOPs, we increased the number of cascades from five to seven in the experiments. For the other networks, we tried our best to preserve the network parameters in their published papers. As shown in the table, ISTA-Net is less computationally complex. However, adding the network parameters did not improve performance. Hence, we retained the announced parameters, as in their study. The corresponding box plots presented in Fig. 4 illustrates the distribution of the results. These results demonstrate that the proposed network can achieve the best performance among the chosen methods without additional computational complexity.

Examples of the reconstructed images from the different methods are plotted in Fig. 5. The first row shows the reconstructed images from the different methods, and the second row shows the corresponding error maps. The error maps can clearly show that our method has the least errors among all methods.

We also evaluated the networks on the selected fastMRI dataset and the results are presented in Table III. With more training and testing data, the experimental results still show that the proposed network achieves superior reconstruction performance, which supports our previous conclusions.

C. Ablation studies

We designed ablation studies to demonstrate the improvements achieved by the proposed modules. The experimental results obtained from the Coronal PD sequence are presented in Table IV. Here, we compared the following five networks:

- addition: The attention-based fusion modules and the correction modules are removed. The mean values of the intermediate results from N_s and N_l are directly fed to the next iterations.
- w/o attention modules: Only the attention-based fusion modules are removed compared with the proposed network. The mean values, instead of the weighted images are fed to the correction modules.
- w/o correction: Only the correction modules are removed from the proposed network, which means that the weighted intermediate results from ATMs are fed to the next iterations.

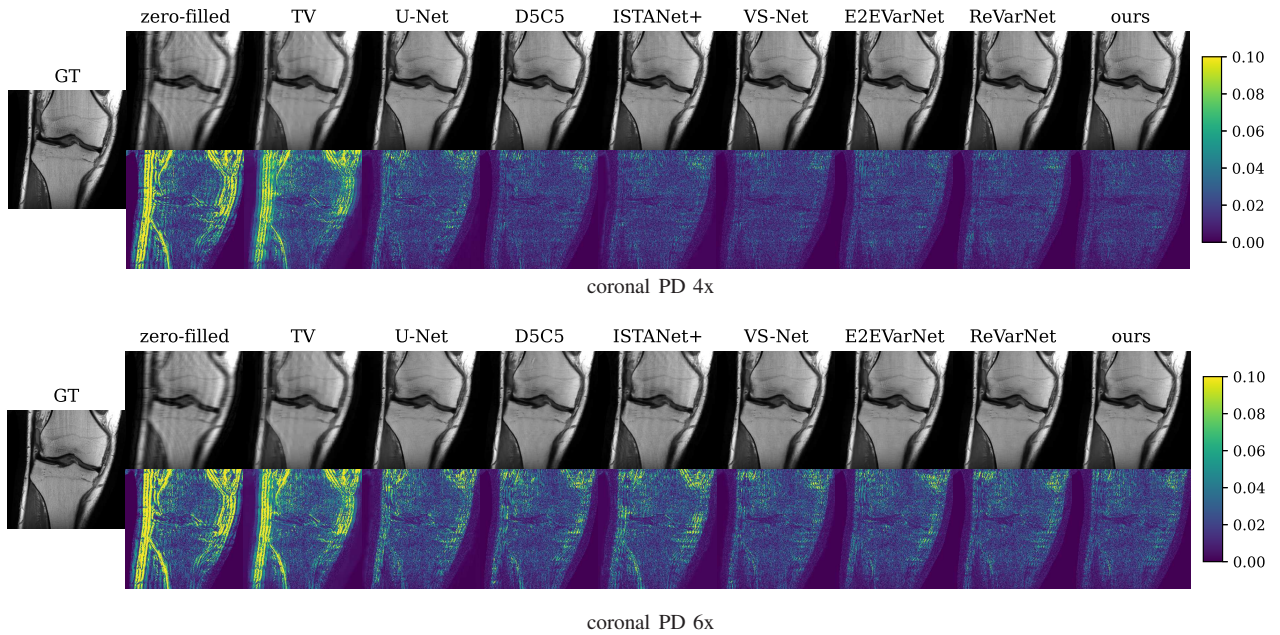


Fig. 5. Example of reconstructed images of different methods. The first row are the reconstructed images of different methods and the second row are the corresponding error maps.

TABLE III
THE QUANTITATIVE RESULTS ON FASTMRI DATASET COMPARED WITH THE STATE-OF-THE-ART METHODS.

Method	PSNR		SSIM	
	4x	6x	4x	6x
zero-filled	32.9685±3.3195	32.1586±3.3248	0.8892±0.0698	0.8719±0.0782
TV	35.0003±2.5388	33.3600±2.4059	0.8848±0.0591	0.8618±0.0672
U-Net	36.7130±3.0727	35.2532±2.9878	0.9196±0.0635	0.8998±0.0719
D5C5	37.8455±3.2348	35.5057±2.9879	0.9302±0.0629	0.9038±0.0717
ISTA-Net	36.9412±3.1956	34.6988±3.0203	0.9236±0.0639	0.8937±0.0725
VS-Net	37.9234±3.2198	35.5370±2.9159	0.9295±0.0618	0.9038±0.0701
E2E-VarNet	38.3504±3.2475	36.0400±2.8785	0.9326±0.0621	0.9081±0.0701
ReVarNet	38.5580±3.2475	36.0142±3.0019	0.9326±0.0621	0.9094±0.0726
CMD-Net (ours)	38.7581±3.3945	36.7581±2.9253	0.9379±0.0630	0.9170±0.0679

- w/o losses: All the intermediate results are not fed to the loss functions. Only the MSE of the final outputs and the ground truth images are incorporate in the loss function.
- ours: The proposed network structure.

All the ablation networks enumerated above follow a parallel network structure (i.e., they include two subnetworks in each cascade). Among these methods, the addition method denotes the simplest parallel network, in which the mean values of the intermediate results from N_s^k and N_l^k are directly fed to the $(k+1)$ th iteration. Compared with the proposed method, the improvement caused by the designed modules is apparent. In Methods 2–4, one module was removed from the proposed network. As shown in the table, deteriorations of varying degrees were observed in the three ablation networks. In other words, only the proposed method with all the designed modules achieved the best results. Moreover, the method without correction modules performed the worst among Methods 2 to 4, which indicates the necessity of this module in the proposed parallel network, that it can effectively enhance the learning ability and eliminate new errors. Moreover, we can observe that the designed modules are easy to apply, the

improvements are obvious, and there is almost no increase in FLOPs.

All the ablation studies in Table IV adopt the proposed parallel network structure, in which different subnetworks leverage different prior knowledge, and the results from the subnetworks are integrated in different ways. We want to further prove that the proposed parallel network structure is better than one prior-based network and that it is a better way to integrate different prior-based subnetworks. Here, we compared the proposed network with two types of networks: (a) one subnetwork is removed. (b) Prior knowledge added to one objective function. For type (a), the computational complexity of these networks should be reduced because the components used to integrate the subnetworks are removed. To eliminate the interference caused by different numbers of network complexity, we added the parameters of type (a) networks so that they can have similar FLOPs as the proposed network. Additionally, we considered that the network depth (i.e., the number of channels) and the number of cascades are two significant parameters that affect the reconstruction performance. Therefore, we tested both methods (i.e., adding

TABLE IV
RESULTS OF ABLATION STUDIES ON CORONAL PD SEQUENCE WITH 4-FOLD AND 6-FOLD ACCELERATION RATES.

Method	MSM	ATM	CM	losses	PSNR		SSIM		FLOPs(G)
					4×	6×	4×	6×	
addition	✓				39.6780	36.9784	0.9528	0.9330	193.05
w/o inter losses	✓	✓	✓		40.6041	37.8079	0.9602	0.9415	204.46
w/o attention	✓		✓	✓	40.7524	37.8623	0.9625	0.9422	201.07
w/o correction	✓	✓		✓	40.2246	37.3507	0.9586	0.9372	196.44
CMD-Net (ours)	✓	✓	✓	✓	40.9309	38.0437	0.9637	0.9438	204.46

TABLE V
RESULTS OF DIFFERENT INTEGRATING METHODS ON CORONAL PD SEQUENCE WITH 4-FOLD AND 6-FOLD ACCELERATION RATES.

Method	PSNR		SSIM		FLOPs(G)
	4×	6×	4×	6×	
L+cascades	40.2784	37.1909	0.9558	0.9296	198.18
L+depth	40.0213	37.3131	0.9556	0.9296	193.08
S+cas+depth	38.7506	35.9477	0.9485	0.9234	228.93
L+S	39.8596	37.5395	0.9552	0.9359	193.05
CMD-Net (ours)	40.9309	38.0437	0.9637	0.9438	204.46

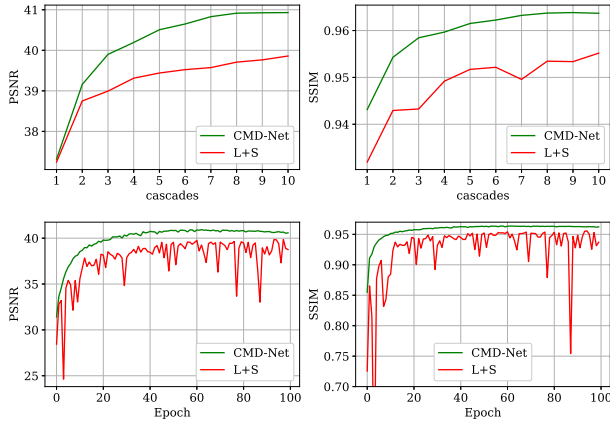


Fig. 6. The comparison between L+S and CMD-Net (ours). The first row: PSNR and SSIM results of the outputs in each cascade. The second row: results on the test set among epoches

the number of cascades or channels) to unify the network complexity.

The designed networks are listed in Table V. In these method names, the capital 'L' denotes the network with only the N_l branch and 'S' with the N_s branch. "+cascades" and "+depth" denote the appropriate addition of the number of channels and cascades in the corresponding networks, respectively. For the L+cascades method, the number of cascades was increased to 16 from 10. For method L+depth, the number of channels in the subnetworks increased from 16 to 20, and from 4 to 8 in the correction modules. For the sparsity based branch, because its FLOPs is relatively lower, merely increasing the cascade or depth makes the network difficult to train. Therefore, we simultaneously increased the number of channels in the learned sparse transform from 32 to 48 and the number of cascades from 10 to 15. Note that L+S in the table solves (22), which is a common method used by existing methods to incorporate two priors. The essential difference between L+S and our method is that the output of

N_l is fed to N_s in L+S and different priors contribute to the results in an alternating form. However, the outputs of N_l and N_s are directly fed into the attention modules in our method to optimize the intermediate results in cascades. As shown in the table, our method outperforms the other methods with 4× and 6× accelerations.

We further compared our method with L+S to show the advantages of the proposed parallel structure. We first plot the PSNR and SSIM results of the outputs in each cascade and the results are shown in the first row of Fig 6. We can observe that the proposed method have a faster convergence, and the output in the third cascade has outperformed the final results in L+S. The second row shows the curves of test results among epoches, and the convergence of the proposed CMD-Net are faster and stabler. The experimental results indicated that the proposed parallel network is a more efficient way to design a model-driven network.

D. Applying to other methods

Another significant advantage of the proposed method is that it can be easily applied to other model-driven methods to improve the results. We first conducted experiments using VS-Net and E2EVarNet. Considering that applying the proposed network design to other unrolling methods will inevitably increase the computational complexity, we tried two ways to unify the FLOPs of different networks: enlarging the original networks or shrinking the designed networks. The experimental results are presented in Table VI. To apply to the VS-Net, we replace the N_s in our Network to VS-Net cascades, and we remark this method as 'VS+L'. We also increase the cascade number in VS-Net from 10 to 15, which is remarked as 'VS-Net+'. We tested the Coronal PD sequence, and as shown in the table, improvements can be observed in 4× and 6× accelerations. We also shrink the designed network for comparison with the original VS-Net, where we use a U-Net to replace the CNN layers in VS-Net. The number of channels in U-Net was set to 16, 32, 64, and 128. The method is remarked as 'VS+L-' in the table, which also outperforms the original VS-Net.

Similarly, the proposed method improved the performance of E2EVarNet. When enlarging the original E2EVarNet, we increased the number of cascades from 12 to 14 and the number of channels in the first layer from 18 to 22. To shrink the designed network, we decreased the number of channels from 16 to 8. We observe similar improvements when applying our methods to E2EVarNet (methods 5–8 in Table VI). In addition, we plotted the 6-fold PSNR values of these methods

TABLE VI
RESULTS OF APPLYING OUR METHOD TO OTHER MODEL-DRIVEN NETWORKS ON CORONAL PD SEQUENCE WITH 4-FOLD AND 6-FOLD ACCELERATION RATES.

Method	PSNR		SSIM		FLOPs(G)
	4x	6x	4x	6x	
VS-Net+	40.4903	37.4789	0.9608	0.9388	398.84
VS+L	40.7765	37.9050	0.9632	0.9433	401.16
VS-Net	40.0622	36.9571	0.9589	0.9348	265.89
VS+L-	40.6820	37.8747	0.9627	0.9427	259.14
E2EVarNet+	38.9097	36.0596	0.9511	0.9273	326.79
E2EVarNet+L	40.6066	37.9044	0.9414	0.9427	310.97
E2EVarNet	39.3592	36.9122	0.9542	0.9344	187.39
E2EVarNet+L-	40.6452	37.7369	0.9616	0.9419	199.93

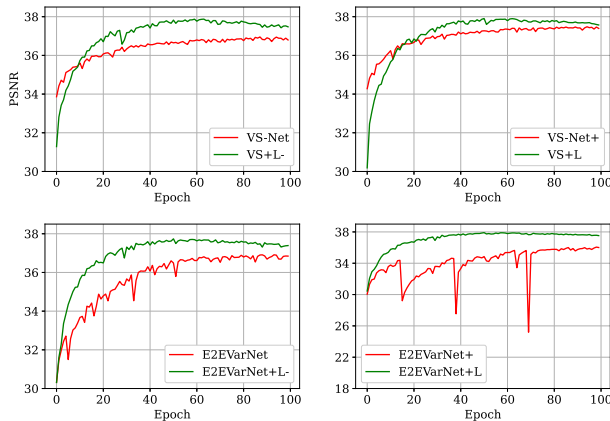


Fig. 7. Test PSNR of different methods at different epoches.

TABLE VII
RESULTS OF APPLYING OUR METHOD TO OTHER MODEL-DRIVEN NETWORKS WHICH BASED ON THE SAME PRIOR.

Method	PSNR		SSIM		FLOPs(G)
	4x	6x	4x	6x	
ISTA+VS	40.8888	38.1022	0.9632	0.9437	204.46
VAR+VS	40.4905	37.8492	0.9615	0.9428	259.14
ISTA+VAR	40.0743	37.4259	0.9592	0.9400	204.46
VS+VS	40.6570	37.7556	0.9626	0.9420	259.14

at different epoches in Fig. 7. The figure clearly shows that our method (the green lines) accelerates the network convergence and improves the performance, and the figures of 4-fold results showed similar results.

E. Subnetworks based on the same priors

All the aforementioned methods adopt subnetworks based on different priors. However, model-driven methods relax the constraints of the conventional algorithms. In other words, prior knowledge in model-driven networks helps to form the network structure, and the networks have more freedom to directly learn from the data compared with conventional methods. Therefore, we explored the possibility of exploiting the complementarity between subnetworks based on the same priors. As the four integrated methods show in Table VII, the integrated networks still outperformed the original networks. Although the final results of the networks are affected by the power of their subnetworks, they prove the effectiveness of our

proposed method. Furthermore, we adopted the same VS-Net for both subnetworks (the final VS+VS method). Although the results were slightly worse than those of the methods based on different subnetworks, they still outperformed the original VS-Net. These results further indicate that the proposed network design is a more efficient method to build model-driven networks than simply stacking unrolled cascades.

V. DISCUSSION

Collaboration is an important idea in medical image reconstruction. For example, massive methods have been proposed to exploit the complementarity between the image domain and raw data domain [59]–[62]. The existing neural networks that combine sparse and low rank priors [48], [63] are essentially based on (22), and few of them, to the best of our knowledge, have explored the best way to organically combine different priors. By comparison, we proposed a novel parallel structure that outperforms the existing methods while it can be easily applied to the other methods.

In this study, we show that an attention-based module is highly important for integrating the intermediate results from different subnetworks. Note that the attention mechanism has been introduced in related reconstruction networks. For example, HUANG [14] *et al.* introduced a variant of U-net with Channel-wise Attention (UCA) module to suppress irrelevant features. In [64], the purpose of attention modules was to adaptively capture local contextual cues. More commonly, attention modules have been introduced into GAN [61], [65]–[67] as indispensable components. However, the essential difference between the aforementioned methods and ours is that we aimed to find the global minima by appropriately integrating our subnetworks.

In this study, we aim to illustrate the superiority of the proposed parallel network structure over the conventional networks which simply stacked cascades. The inputs for the attention modules are the 2-channel intermediate results from subnetworks. The reason is that we aim to design a universal model-driven network structure, which can be easily applied to the other methods without complicated adjustment to their network. Meanwhile, it is more intuitive to directly learn the attention maps from features instead of from reconstructed images, and more information can be preserved. Here, we further explored the possibility to learn the attention maps from features. We remove the last convolutional layers in Fig. 2 (b) and (c), which learn the 2-channel intermediate outputs from 32-channel features. Then, the features are concatenated and fed to the attention blocks to learn new attention maps. Considering the increase in the number of channels, we add a simple channel-wise attention (CWA) block to grant more weights to significant features. The new structure of the attention blocks are shown in Fig. 8. The other network structures in CMD-Net are preserved, and we compare the new network, dubbed as CMD-Net⁺ with CMD-Net. We can still observe slight improvements from the reconstruction results, indicating that the proposed network has potential to improve with richer input features. However, considering that our training dataset is relatively small, and more training data

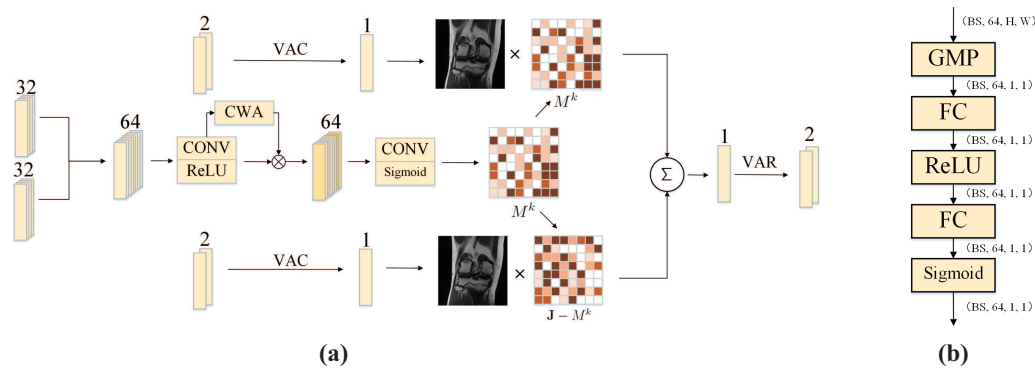


Fig. 8. (a) An optimized attention module with richer input features. (b) The structure of the CWA block. GMP: global maximum pooling.

is required to fit a neural network with more parameters, in future works we aim to conduct experiments on larger dataset to prove the feasibility when applying to more complex priors and network design.

VI. CONCLUSION

In this study, we designed a collaborative model-driven network that integrates different prior knowledge to achieve better performance. We adopted simple backbone networks based on low rankness and sparsity, which yielded superior results. When applied to other model-driven methods, clear improvements were observed without additional computational complexity.

- [1] M. G. Harisinghani, A. O'Shea, and R. Weissleder, "Advances in clinical mri technology," *Science Translational Medicine*, vol. 11, no. 523, p. eaba2591, 2019.
- [2] D. Larkman and R. Nunes, "Parallel magnetic resonance imaging," *Phys Med Biol*, vol. 52, no. 7, p. R15, 2007.
- [3] K. Pruessmann, M. Weiger, M. Scheidegger, and P. Boesiger, "Sense: sensitivity encoding for fast mri," *Magn Reson Med*, vol. 42, no. 5, pp. 952–962, 1999.
- [4] M. A. Griswold, P. M. Jakob, R. M. Heidemann, M. Nittka, V. Jellus, J. Wang, B. Kiefer, and A. Haase, "Generalized autocalibrating partially parallel acquisitions (grappa)," *Magnetic Resonance in Medicine: An Official Journal of the International Society for Magnetic Resonance in Medicine*, vol. 47, no. 6, pp. 1202–1210, 2002.
- [5] D. L. Donoho, "Compressed sensing," *IEEE Transactions on information theory*, vol. 52, no. 4, pp. 1289–1306, 2006.
- [6] W. Wu, D. Hu, K. An, S. Wang, and F. Luo, "A high-quality photon-counting ct technique based on weight adaptive total-variation and image-spectral tensor factorization for small animals imaging," *IEEE Transactions on Instrumentation and Measurement*, vol. 70, pp. 1–14, 2020.
- [7] M. Lustig, D. Donoho, and J. M. Pauly, "Sparse mri: The application of compressed sensing for rapid mr imaging," *Magnetic Resonance in Medicine: An Official Journal of the International Society for Magnetic Resonance in Medicine*, vol. 58, no. 6, pp. 1182–1195, 2007.
- [8] M. Lustig, D. L. Donoho, J. M. Santos, and J. M. Pauly, "Compressed sensing mri," *IEEE signal processing magazine*, vol. 25, no. 2, pp. 72–82, 2008.
- [9] K. Hollingsworth, "Reducing acquisition time in clinical mri by data undersampling and compressed sensing reconstruction," *Phys Med Biol*, vol. 60, no. 21, p. R297, 2015.
- [10] X. Qu, W. Zhang, D. Guo, C. Cai, S. Cai, and Z. Chen, "Iterative thresholding compressed sensing mri based on contourlet transform," *Inverse Probl Sci En*, vol. 18, no. 6, pp. 737–758, 2010.
- [11] S. Wang, T. Xiao, Q. Liu, and H. Zheng, "Deep learning for fast mr imaging: A review for learning reconstruction from incomplete k-space data," *Biomedical Signal Processing and Control*, vol. 68, p. 102579, 2021.
- [12] G. Yang, S. Yu, H. Dong, G. Slabaugh, P. L. Dragotti, X. Ye, F. Liu, S. Arridge, J. Keegan, Y. Guo et al., "Dagan: Deep de-aliasing generative adversarial networks for fast compressed sensing mri reconstruction," *IEEE transactions on medical imaging*, vol. 37, no. 6, pp. 1310–1321, 2017.
- [13] S. Wang, H. Cheng, L. Ying, T. Xiao, Z. Ke, H. Zheng, and D. Liang, "Deepcomplexmri: Exploiting deep residual network for fast parallel mr imaging with complex convolution," *Magnetic Resonance Imaging*, vol. 68, pp. 136–147, 2020.
- [14] Q. Huang, D. Yang, P. Wu, H. Qu, J. Yi, and D. Metaxas, "Mri reconstruction via cascaded channel-wise attention network," in *2019 IEEE 16th International Symposium on Biomedical Imaging (ISBI 2019)*. IEEE, 2019, pp. 1622–1626.
- [15] M. Akçakaya, S. Moeller, S. Weingärtner, and K. Uğurbil, "Scan-specific robust artificial-neural-networks for k-space interpolation (raki) reconstruction: Database-free deep learning for fast imaging," *Magnetic resonance in medicine*, vol. 81, no. 1, pp. 439–453, 2019.
- [16] M. Mardani, E. Gong, J. Y. Cheng, S. S. Vasanawala, G. Zaharchuk, L. Xing, and J. M. Pauly, "Deep generative adversarial neural networks for compressive sensing mri," *IEEE transactions on medical imaging*, vol. 38, no. 1, pp. 167–179, 2018.
- [17] T. M. Quan, T. Nguyen-Duc, and W.-K. Jeong, "Compressed sensing mri reconstruction using a generative adversarial network with a cyclic loss," *IEEE transactions on medical imaging*, vol. 37, no. 6, pp. 1488–1497, 2018.
- [18] D. Hu, Y. Zhang, J. Zhu, Q. Liu, and Y. Chen, "Trans-net: Transformer-enhanced residual-error alternative suppression network for mri reconstruction," *IEEE Transactions on Instrumentation and Measurement*, vol. 71, pp. 1–13, 2022.
- [19] J. Zhang and B. Ghanem, "Ista-net: Interpretable optimization-inspired deep network for image compressive sensing," in *Proceedings of the IEEE conference on computer vision and pattern recognition*, 2018, pp. 1828–1837.
- [20] J. Duan, J. Schlemper, C. Qin, C. Ouyang, W. Bai, C. Biffi, G. Bello, B. Statton, D. P. O'regan, and D. Rueckert, "Vs-net: Variable splitting network for accelerated parallel mri reconstruction," in *Medical Image Computing and Computer Assisted Intervention—MICCAI 2019: 22nd International Conference, Shenzhen, China, October 13–17, 2019, Proceedings, Part IV 22*. Springer, 2019, pp. 713–722.
- [21] A. Sriram, J. Zbontar, T. Murrell, A. Defazio, C. L. Zitnick, N. Yakubova, F. Knoll, and P. Johnson, "End-to-end variational networks for accelerated mri reconstruction," in *Medical Image Computing and Computer Assisted Intervention—MICCAI 2020: 23rd International Conference, Lima, Peru, October 4–8, 2020, Proceedings, Part II 23*. Springer, 2020, pp. 64–73.
- [22] K. Hammernik, T. Klatzer, E. Kobler, M. P. Recht, D. K. Sodickson, T. Pock, and F. Knoll, "Learning a variational network for reconstruction of accelerated mri data," *Magnetic resonance in medicine*, vol. 79, no. 6, pp. 3055–3071, 2018.
- [23] G. Yiasemis, J.-J. Sonke, C. Sánchez, and J. Teuwen, "Recurrent variational network: a deep learning inverse problem solver applied to the task of accelerated mri reconstruction," in *Proceedings of the IEEE/CVF Conference on Computer Vision and Pattern Recognition*, 2022, pp. 732–741.
- [24] E. Z. Chen, P. Wang, X. Chen, T. Chen, and S. Sun, "Pyramid convolutional rnn for mri image reconstruction," *IEEE Transactions on Medical Imaging*, vol. 41, no. 8, pp. 2033–2047, 2022.

- [25] Z. Ramzi, G. Chaithya, J.-L. Starck, and P. Ciuciu, "Nc-pdnet: A density-compensated unrolled network for 2d and 3d non-cartesian mri reconstruction," *IEEE Transactions on Medical Imaging*, vol. 41, no. 7, pp. 1625–1638, 2022.
- [26] H. K. Aggarwal, M. P. Mani, and M. Jacob, "Modl: Model-based deep learning architecture for inverse problems," *IEEE transactions on medical imaging*, vol. 38, no. 2, pp. 394–405, 2018.
- [27] Y. Jun, H. Shin, T. Eo, and D. Hwang, "Joint deep model-based mr image and coil sensitivity reconstruction network (joint-icnet) for fast mri," in *Proceedings of the IEEE/CVF Conference on Computer Vision and Pattern Recognition*, 2021, pp. 5270–5279.
- [28] T. Lu, X. Zhang, Y. Huang, D. Guo, F. Huang, Q. Xu, Y. Hu, L. Ou-Yang, J. Lin, Z. Yan *et al.*, "pista-sense-resnet for parallel mri reconstruction," *Journal of Magnetic Resonance*, vol. 318, p. 106790, 2020.
- [29] J. Sun, H. Li, Z. Xu *et al.*, "Deep admm-net for compressive sensing mri," *Advances in neural information processing systems*, vol. 29, 2016.
- [30] A. Beck and M. Teboulle, "A fast iterative shrinkage-thresholding algorithm for linear inverse problems," *SIAM journal on imaging sciences*, vol. 2, no. 1, pp. 183–202, 2009.
- [31] Y. Yang and J. Jia, "An image reconstruction algorithm for electrical impedance tomography using adaptive group sparsity constraint," *IEEE Transactions on Instrumentation and Measurement*, vol. 66, no. 9, pp. 2295–2305, 2017.
- [32] S. Wang, H. Yu, Y. Xi, C. Gong, W. Wu, and F. Liu, "Spectral-image decomposition with energy-fusion sensing for spectral ct reconstruction," *IEEE Transactions on Instrumentation and Measurement*, vol. 70, pp. 1–11, 2021.
- [33] J. Ye, H. Wang, and W. Yang, "Image recovery for electrical capacitance tomography based on low-rank decomposition," *IEEE Transactions on Instrumentation and Measurement*, vol. 66, no. 7, pp. 1751–1759, 2017.
- [34] T. Qiu, W. Liao, Y. Huang, J. Wu, D. Guo, D. Liu, X. Wang, J.-F. Cai, B. Hu, and X. Qu, "An automatic denoising method for nmr spectroscopy based on low-rank hankel model," *IEEE Transactions on Instrumentation and Measurement*, vol. 70, pp. 1–12, 2021.
- [35] Z. Ke, W. Huang, Z.-X. Cui, J. Cheng, S. Jia, H. Wang, X. Liu, H. Zheng, L. Ying, Y. Zhu *et al.*, "Learned low-rank priors in dynamic mr imaging," *IEEE Transactions on Medical Imaging*, vol. 40, no. 12, pp. 3698–3710, 2021.
- [36] X. Zhang, D. Guo, Y. Huang, Y. Chen, L. Wang, F. Huang, Q. Xu, and X. Qu, "Image reconstruction with low-rankness and self-consistency of k-space data in parallel mri," *Medical Image Analysis*, vol. 63, p. 101687, 2020.
- [37] K. H. Jin, D. Lee, and J. C. Ye, "A general framework for compressed sensing and parallel mri using annihilating filter based low-rank hankel matrix," *IEEE Transactions on Computational Imaging*, vol. 2, no. 4, pp. 480–495, 2016.
- [38] M. Jacob, M. P. Mani, and J. C. Ye, "Structured low-rank algorithms: Theory, magnetic resonance applications, and links to machine learning," *IEEE signal processing magazine*, vol. 37, no. 1, pp. 54–68, 2020.
- [39] A. Pramanik, H. K. Aggarwal, and M. Jacob, "Deep generalization of structured low-rank algorithms (deep-slr)," *IEEE transactions on medical imaging*, vol. 39, no. 12, pp. 4186–4197, 2020.
- [40] X. Zhang, H. Lu, D. Guo, Z. Lai, H. Ye, X. Peng, B. Zhao, and X. Qu, "Accelerated mri reconstruction with separable and enhanced low-rank hankel regularization," *IEEE Transactions on Medical Imaging*, vol. 41, no. 9, pp. 2486–2498, 2022.
- [41] Z. Wang, C. Qian, D. Guo, H. Sun, R. Li, B. Zhao, and X. Qu, "One-dimensional deep low-rank and sparse network for accelerated mri," *IEEE Transactions on Medical Imaging*, vol. 42, no. 1, pp. 79–90, 2022.
- [42] X. Qu, M. Mayzel, J.-F. Cai, Z. Chen, and V. Orekhov, "Accelerated nmr spectroscopy with low-rank reconstruction," *Angewandte Chemie International Edition*, vol. 54, no. 3, pp. 852–854, 2015.
- [43] Y. Huang, J. Zhao, Z. Wang, V. Orekhov, D. Guo, and X. Qu, "Exponential signal reconstruction with deep hankel matrix factorization," *IEEE Transactions on Neural Networks and Learning Systems*, 2021.
- [44] N. Srebro, "Learning with matrix factorizations," *massachusetts institute of technology*, 2004.
- [45] S. Boyd, N. Parikh, E. Chu, B. Peleato, J. Eckstein *et al.*, "Distributed optimization and statistical learning via the alternating direction method of multipliers," *Foundations and Trends® in Machine Learning*, vol. 3, no. 1, pp. 1–122, 2011.
- [46] S. G. Lingala, Y. Hu, E. DiBella, and M. Jacob, "Accelerated dynamic mri exploiting sparsity and low-rank structure: kt slr," *IEEE transactions on medical imaging*, vol. 30, no. 5, pp. 1042–1054, 2011.
- [47] R. Otazo, E. Candes, and D. K. Sodickson, "Low-rank plus sparse matrix decomposition for accelerated dynamic mri with separation of background and dynamic components," *Magnetic resonance in medicine*, vol. 73, no. 3, pp. 1125–1136, 2015.
- [48] C. Y. Lin and J. A. Fessler, "Efficient dynamic parallel mri reconstruction for the low-rank plus sparse model," *IEEE transactions on computational imaging*, vol. 5, no. 1, pp. 17–26, 2018.
- [49] A. Majumdar, R. K. Ward, and T. Aboulnasr, "Non-convex algorithm for sparse and low-rank recovery: Application to dynamic mri reconstruction," *Magnetic resonance imaging*, vol. 31, no. 3, pp. 448–455, 2013.
- [50] M. Arvinte, S. Vishwanath, A. H. Tewfik, and J. I. Tamir, "Deep j-sense: Accelerated mri reconstruction via unrolled alternating optimization," in *International conference on medical image computing and computer-assisted intervention*. Springer, 2021, pp. 350–360.
- [51] K. Mohan and M. Fazel, "Iterative reweighted algorithms for matrix rank minimization," *The Journal of Machine Learning Research*, vol. 13, no. 1, pp. 3441–3473, 2012.
- [52] Y. Liu, Z. Zhan, J.-F. Cai, D. Guo, Z. Chen, and X. Qu, "Projected iterative soft-thresholding algorithm for tight frames in compressed sensing magnetic resonance imaging," *IEEE transactions on medical imaging*, vol. 35, no. 9, pp. 2130–2140, 2016.
- [53] X. Zhang, H. Lu, D. Guo, L. Bao, F. Huang, Q. Xu, and X. Qu, "A guaranteed convergence analysis for the projected fast iterative soft-thresholding algorithm in parallel mri," *Medical Image Analysis*, vol. 69, p. 101987, 2021.
- [54] J. Zbontar, F. Knoll, A. Sriram, T. Murrell, Z. Huang, M. J. Muckley, A. Defazio, R. Stern, P. Johnson, M. Bruno *et al.*, "fastmri: An open dataset and benchmarks for accelerated mri," *arXiv preprint arXiv:1811.08839*, 2018.
- [55] M. Uecker, P. Lai, M. J. Murphy, P. Virtue, M. Elad, J. M. Pauly, S. S. Vasanawala, and M. Lustig, "Espirit—an eigenvalue approach to autocalibrating parallel mri: where sense meets grappa," *Magnetic resonance in medicine*, vol. 71, no. 3, pp. 990–1001, 2014.
- [56] F. Ong and M. Lustig, "Sigpy: a python package for high performance iterative reconstruction," in *Proceedings of the ISMRM 27th Annual Meeting, Montreal, Quebec, Canada*, vol. 4819, no. 5, 2019.
- [57] S. Ma, W. Yin, Y. Zhang, and A. Chakraborty, "An efficient algorithm for compressed mr imaging using total variation and wavelets," in *2008 IEEE Conference on Computer Vision and Pattern Recognition*. IEEE, 2008, pp. 1–8.
- [58] J. Schlemper, J. Caballero, J. V. Hajnal, A. Price, and D. Rueckert, "A deep cascade of convolutional neural networks for mr image reconstruction," in *Information Processing in Medical Imaging: 25th International Conference, IPMI 2017, Boone, NC, USA, June 25-30, 2017, Proceedings 25*. Springer, 2017, pp. 647–658.
- [59] C. Wang, K. Shang, H. Zhang, Q. Li, Y. Hui, and S. K. Zhou, "Dudotrans: dual-domain transformer provides more attention for sinogram restoration in sparse-view ct reconstruction," *arXiv preprint arXiv:2111.10790*, 2021.
- [60] R. Ge, Y. He, C. Xia, H. Sun, Y. Zhang, D. Hu, S. Chen, Y. Chen, S. Li, and D. Zhang, "Ddpnet: A novel dual-domain parallel network for low-dose ct reconstruction," in *International Conference on Medical Image Computing and Computer-Assisted Intervention*. Springer, 2022, pp. 748–757.
- [61] X. Liu, Y. Pang, R. Jin, Y. Liu, and Z. Wang, "Dual-domain reconstruction network with v-net and k-net for fast mri," *Magnetic Resonance in Medicine*, vol. 88, no. 6, pp. 2694–2708, 2022.
- [62] T. Eo, Y. Jun, T. Kim, J. Jang, H.-J. Lee, and D. Hwang, "Kiki-net: cross-domain convolutional neural networks for reconstructing undersampled magnetic resonance images," *Magnetic resonance in medicine*, vol. 80, no. 5, pp. 2188–2201, 2018.
- [63] W. Huang, Z. Ke, Z.-X. Cui, J. Cheng, Z. Qiu, S. Jia, L. Ying, Y. Zhu, and D. Liang, "Deep low-rank plus sparse network for dynamic mr imaging," *Medical Image Analysis*, vol. 73, p. 102190, 2021.
- [64] J. Liu, C. Qin, and M. Yaghoobi, "Coil-agnostic attention-based network for parallel mri reconstruction," in *Proceedings of the Asian Conference on Computer Vision*, 2022, pp. 2866–2883.
- [65] Z. Yuan, M. Jiang, Y. Wang, B. Wei, Y. Li, P. Wang, W. Menpes-Smith, Z. Niu, and G. Yang, "Sara-gan: Self-attention and relative average discriminator based generative adversarial networks for fast compressed sensing mri reconstruction," *Frontiers in Neuroinformatics*, vol. 14, p. 611666, 2020.
- [66] Y. Wu, Y. Ma, J. Liu, J. Du, and L. Xing, "Self-attention convolutional neural network for improved mr image reconstruction," *Information sciences*, vol. 490, pp. 317–328, 2019.
- [67] W. Zhou, H. Du, W. Mei, and L. Fang, "Spatial orthogonal attention generative adversarial network for mri reconstruction," *Medical Physics*, vol. 48, no. 2, pp. 627–639, 2021.